

Incorporating intratumoral heterogeneity into weakly-supervised deep learning models via variance pooling

Iain Carmichael*, Andrew H. Song*, Richard J. Chen, Drew F.K. Williamson, Tiffany Y. Chen, and Faisal Mahmood

Department of Pathology, Brigham and Women’s Hospital, Harvard Medical School, Boston, MA

Department of Pathology, Massachusetts General Hospital, Harvard Medical School, Boston, MA

{icarmichael, asong, rchen14, dwilliamson, tchen25, faisalmahmood}@bwh.harvard.edu

Abstract. Supervised learning tasks such as cancer survival prediction from gigapixel whole slide images (WSIs) are a critical challenge in computational pathology that requires modeling complex features of the tumor microenvironment. These learning tasks are often solved with deep multi-instance learning (MIL) models that do not explicitly capture intratumoral heterogeneity. We develop a novel variance pooling architecture that enables a MIL model to incorporate intratumoral heterogeneity into its predictions. Two interpretability tools based on “representative patches” are illustrated to probe the biological signals captured by these models. An empirical study with 4,479 gigapixel WSIs from the Cancer Genome Atlas shows that adding variance pooling onto MIL frameworks improves survival prediction performance for five cancer types.

Keywords: Computer Vision, Computational Pathology, Multiple Instance Learning, Intratumoral Heterogeneity, Interpretability

1 Introduction

Cancer diagnosis and prognosis using *hematoxylin and eosin* (H&E) stained *whole slide images* (WSIs) are central tasks in computational pathology. These supervised learning problems are made difficult by the size and complexity of WSIs; these images can be gigapixels in scale and involve localizing subtle visual signals that expert pathologists are trained for years to identify. In recent years, weakly supervised deep learning algorithms have made significant progress in addressing some of these challenges [Campanella et al., 2019, Coudray et al., 2018, Courtiol et al., 2019, Couture et al., 2018, Lu et al., 2021, Wulczyn et al., 2021].

* These authors contributed equally

Cancer cell morphology can vary greatly within a single tumor and it is increasingly recognized that *intratumoral heterogeneity* (ITH) plays an important role in prognostication for certain cancer types [Andor et al., 2016, Marusyk et al., 2020], though its exact role is still being elucidated. Furthermore, ITH complicates prognostication based on WSIs by increasing the range of morphologies that correspond to a particular prognosis. For example, pathologists often encounter *clear cell renal cell carcinoma* displaying significant heterogeneity within the same tumor, with some areas demonstrating classic clear cell morphology and others displaying morphologies bordering on diagnoses such as *chromophobe renal cell carcinoma* or *clear cell tubulopapillary renal cell carcinoma*.

Existing supervised algorithms that scale to WSIs do not generally incorporate histological ITH. These algorithms typically approach a supervised learning task such as survival prediction through a *multiple instance learning* (MIL) framework [Ilse et al., 2018]. First, a WSI is represented as a *bag* of many smaller image patches. Next, neural network features are extracted from each patch. Finally, these patch features are aggregated for prediction. The standard MIL aggregation approaches capture only simple statistics (e.g. mean or max) and neglect higher-order information (e.g. variance), which can capture heterogeneity.

To this end, we develop a novel MIL aggregation component that scales to gigapixel WSIs and explicitly incorporates ITH into its predictions. We accomplish this through a *variance pooling* operation that quantifies ITH as the variance along a collection of low rank projections of patch features (Section 2.2). Moving beyond pre-specified measures of heterogeneity (e.g. the variance of tumor cell morphology), this architecture uses the data to determine how to measure heterogeneity (e.g. the projection vectors, along which the variance of the features are measured, are learned.) This operation can be seamlessly incorporated into existing MIL architectures, as we now demonstrate.

We demonstrate empirically in Section 3 that including this operation improves baseline MIL models’ performance on survival prediction tasks across five cancer types from The Cancer Genome Atlas (TCGA). Through attention and a novel “variance projection contrast” visualization, we provide interpretable insights into what biological signals these architectures utilize to make the predictions in Section 4. Code: <https://github.com/mahmoodlab/VARPOOL>.

1.1 Related Work

Survival Analysis using WSIs: Survival analysis in histopathology has been a longstanding problem in medical imaging. Early work required manual identification of regions of interest [Gurcan et al., 2009]. Other methods make use of hand-crafted tumor cell features (e.g. shape) to predict patient survival [Lu et al., 2018]. Most recent survival methods use MIL algorithms that are directly trained on WSIs without additional annotations [Mobadersany et al., 2018, Wulczyn et al., 2021, Zhao et al., 2020, Zhu et al., 2017]. Some of these methods use *graph convolutional networks* (GCNs), which learn more context-aware features [Chen et al., 2021, Zhao et al., 2020].

Intratumoral Heterogeneity: Much of the previous work on ITH uses genomic data to identify and quantify subclones of tumor cells that share mutations [Raynaud et al., 2018]. There is growing interest in using machine learning to quantify the histologic ITH that pathologists observe on a daily basis [Faust et al., 2020].

2 Incorporating heterogeneity with variance pooling

This section presents the novel variance pooling operation for weakly-supervised MIL tasks. In this setting, we observe a set of bags – an unordered collection of vectors (instances) – that we use to predict some bag level response. In computational pathology, each patient has a WSI which is used to predict the response (e.g. class label or survival outcome). Each patient’s WSI¹ (the bag) is broken up into many small image patches and the instances are either the raw image patches or patch features extracted by a neural network.

We first define some notation. Suppose we have N patients. For the i th patient, we observe a response $y^{(i)}$ and a bag of instances (image patch features) $\mathcal{X}^{(i)} = \{x_1^{(i)}, \dots, x_{n^{(i)}}^{(i)}\}$, where each $x_j^{(i)} \in \mathbb{R}^d$ and $n^{(i)}$ is the size of the bag. For classification tasks $y^{(i)}$ is a patient-level class label; for survival tasks $y^{(i)} = (t^{(i)}, c^{(i)})$ where $t^{(i)} \in \mathbb{R}_+$ is the observed survival time and $c^{(i)} \in \{0, 1\}$ indicates whether or not this time was censored. We want to learn a mapping $f(\mathcal{X}^{(i)}) = z^{(i)}$ that outputs a patient-level prediction minimizing a supervised loss function.

In the following two sections, we present the variance pool architecture in the context of the attention mean pooling model of Ilse et al. [2018]. We emphasize variance pooling can be easily incorporated into other MIL architectures. For notational simplicity we generally drop the patient superscript i .

2.1 Attention mean pooling architecture

The attention mean pool architecture of Ilse et al. [2018] reduces a bag of instances, $\{x_j\}_{j=1}^n$, to a vector through a weighted mean operation. Specifically, each instance is first passed through an (optional) encoding network, as $h_j = \phi(x_j) \in \mathbb{R}^{d_{\text{enc}}}$. The attention neural network α , takes in $\{h_j\}_{j=1}^n$ and computes the normalized attention weights $a = \alpha(\{h_j\}_{j=1}^n) \in \mathbb{R}_+^n$, which sum to 1. The attention mean pool vector p_{mean} is obtained as

$$p_{\text{mean}} = \sum_{j=1}^n a_j h_j. \quad (1)$$

Finally, the bag prediction (e.g. predicted survival risk) is obtained by passing p_{mean} through an additional multi-layer perceptron (MLP), $z = \rho(p_{\text{mean}})$.

¹ When a patient has multiple WSIs, the patches are unioned across the WSIs.

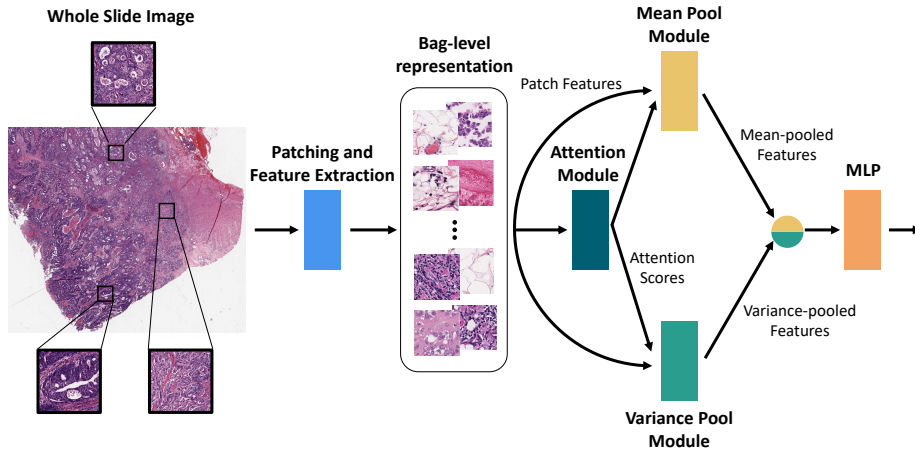


Fig. 1: Variance pooling framework. Zoomed-in WSI patches show examples of intratumoral heterogeneity, with the colonic adenocarcinoma displaying multiple moderately- to poorly-differentiated morphologies. The mean and variance pooling branches capture different statistical characteristics of the data and are aggregated to yield the final prediction.

2.2 Attention variance pooling

We incorporate within-bag heterogeneity (intratumoral heterogeneity) by computing the variance of learned projections of the instances. First, let us define the *attention variance function*, $\text{Var}(\cdot; a) : \mathbb{R}^n \rightarrow \mathbb{R}$, of n numbers, $u \in \mathbb{R}^n$, as

$$\text{Var}(u; a) := \sum_{j=1}^n a_j \left(u_j - \sum_{\ell=1}^n a_\ell u_\ell \right)^2 \quad (2)$$

with attention weights $a \in \mathbb{R}_+^n$ summing to one. Note, if the attention weights are all equal this is the empirical variance of the entries of u .

We then define a K -dimensional variance pool of $\{h_j\}_{j=1}^n$ as follows. Let $v_k \in \mathbb{R}^{d_{\text{enc}}}$, $k \in [K] := \{1, \dots, K\}$, be variance projection vectors, which are learnable parameters in the network. Denote the matrix of encoded instance features as $H \in \mathbb{R}^{n \times d_{\text{enc}}}$, i.e. the j th row of H is given by h_j . The k th entry² of the variance pool vector $p_{\text{var}} \in \mathbb{R}_+^K$ is obtained as

$$p_{\text{var},k} = \text{Var}(Hv_k; \alpha) = \sum_{j=1}^n a_j \left(h_j^T v_k - \sum_{\ell=1}^n a_\ell h_\ell^T v_k \right)^2. \quad (3)$$

This can be viewed as dimensionality reduction on the (attention weighted) covariance matrix of H , i.e., from $O(d_{\text{enc}}^2)$ to K .

² Without the attention weights this would be the quadratic form $v_k^T \text{cov}(H)v_k$.

We pass p_{var} through an entrywise non-linearity, $\eta(\cdot)$, such as $\sqrt{\cdot}$ or $\log(\epsilon + \cdot)$. This non-linearity operation is required since linear combinations of several variance pools is equivalent to just a single variance pool. Finally, the first and second moment information of the attended $\{h_j\}_{j=1}^n$ are combined and the prediction is obtained by passing the concatenated mean and variance pool vector,

$$p_{\text{cat}} = [p_{\text{mean}}; \eta(p_{\text{var}})] \in \mathbb{R}^{d_{\text{enc}} + K} \quad (4)$$

through the MLP, $z = \rho(p_{\text{cat}})$ ³.

Figure 1 shows the entire architecture. The learnable parameters are the networks $\{\phi, \alpha, \rho\}$ and $\{v_k\}_{k=1}^K$. Several design choices can be modified including: no attention mechanism, separate attention mechanisms for the mean and variance pools, and different combination schemes for the mean/variance pools.

3 Experiments with survival prediction

Data: From the public TCGA dataset, we use: Breast Invasive Carcinoma (BRCA, $N = 1,061$), Glioblastoma & Lower Grade Glioma (GBMLGG, $N = 872$), Uterine Corpus Endometrial Carcinoma (UCEC, $N = 504$), Colon Adenocarcinoma & Rectum Adenocarcinoma (COADREAD, $N = 612$), and Bladder Urothelial Carcinoma (BLCA, $N = 386$). The choice of these types was based on the number of patients. We use *progression-free interval* (PFI) [Liu et al., 2018].

We use the concordance index (c-Index) to evaluate survival prediction models. The c-Index, which lies between 0 and 1 (larger is better), measures the agreement between predicted risk scores and actual survival outcomes using only order information (see discussion around (5) below.) We split each dataset into a 70%/30% train/test split. To ensure that our results are not sensitive to a particular data split, we randomly split the data into train/test folds 10 times.

Implementation Details: We extract $d = 1,024$ features from each WSI image patch (256×256 pixels at $20\times$ magnification) using an ImageNet-pretrained ResNet-50 CNN encoder, truncated after the third residual block and spatially averaged. We use a batch size of $B = 32$ patients⁴. To fit each mini-batch into GPU memory during training we cap-by random subsampling- the number of instances in each bag. For each cancer type, the maximum number of instances per bag is set to be the 75% quantile of the overall bag sizes (WSIs typically have 15 – 20,000 patches). In the Supplemental information, we report the summary statistics for number of instances per WSI slide in the TCGA dataset. All patches

³ A similar approach, which we were unaware of until after publication, has been successfully used for microsatellite instability (MSI) prediction Schirris et al. [2022]. This approach is most related to variance pooling with $K=d$ and the variance projection coefficients fixed to be the standard basis vectors.

⁴ Note the patient batch size is not equal to the number of summands in (5); there are between 0 and $\binom{B}{2}$ summands depending on the number of comparable pairs.

in the bag are used at test time. We use the Adam optimizer with a learning rate of 2×10^{-4} , weight decay of 1×10^{-5} , and train for 30 epochs.

We use three MIL architectures: Deep Sets [Zaheer et al., 2017], Attention MeanPool [Ilse et al., 2018], and DeepGraphConv [Zhao et al., 2020]. For the Deep Sets framework, the attention weights are not learned and instead set to identical values of $1/n$. For the DeepGraphConv framework, the bag of features is first passed through two layers of graph convolutional neural network layers, the output of which are passed through the attention mean/variance pooling modules. These are some of the most popular MIL architectures used in computational pathology and thus provide great testbeds for variance pooling module extension.

We use $K = 10$ variance pooling projections and an $\eta(\cdot) = \log(0.01 + \cdot)$ non-linearity. We performed an internal ablation study for the nonlinearity comparing the logarithm, square root, and sigmoid functions, but did not find any significant difference in performance. We initialize the projection vectors $v_k \sim \mathcal{N}(0, 1/d_{\text{enc}})$ to make them approximately orthonormal with high probability.

Loss function: Suppose the bag prediction network, $f(\cdot)$, outputs a risk score for each patient. We train the network with the survival ranking loss [Luck et al., 2018, Steck et al., 2007], which is a continuous approximation of the negative c-Index given by

$$\mathcal{L}(\{\mathcal{X}^{(i)}, t^{(i)}, c^{(i)}\}_{i=1}^N) = -\frac{1}{|\mathcal{C}|} \sum_{(w,b) \in \mathcal{C}} \psi(f(\mathcal{X}^{(w)}) - f(\mathcal{X}^{(b)})), \quad (5)$$

where $\mathcal{C} = \{(w, b) | c^{(w)} = 0 \text{ and } t^{(w)} < t^{(b)}, \text{ for } w, b \in [N]\}$ is the set of *comparable pairs* i.e. pairs of patients where we know one patient has worse survival than the other. If $\psi(\cdot) = \mathbf{1}(\cdot > 0)$ then (5) would be exactly the negative c-Index. We set $\psi(\cdot)$ to be a sigmoid, which is a differentiable approximation of this indicator.

We chose the ranking loss because it is separable, which allows the use of proper mini-batches unlike the Cox loss. Additionally, the c-Index is a natural objective for survival analysis. An alternative is the negative log-likelihood of a discrete time-to-event model [Zadeh and Schmid, 2020]. This loss function coarsely bins the survival times and does not fully utilize the available survival ordering information.

Table 1 shows the results. We observe that for every cancer type and all models, the variance pooling versions outperform their counterparts, with up to 10.4% relative increase (Deep Sets for COADREAD). We conjecture that the smaller performance gain in DeepGraphConv comes from “feature smoothing” in GCNs, which reduces the heterogeneity in patch features. In the Supplemental information, we present an ablation study with the Cox loss and show that similar improvements are observed with the addition of variance pooling module.

The fact that explicitly incorporating intratumoral heterogeneity gives the greatest benefit in COADREAD and UCEC is interesting, since subsets of these tumor types have very high mutation rates due to microsatellite instability, a molecular change with impacts on survival [Guinney et al., 2015, Levine, 2013].

Table 1: Test set c-Index performance (mean \pm std) across 10 re-sampled data splits on the 100 point scale.

Frameworks	BRCA	GBMLGG	COADREAD
Deep Sets	59.5 \pm 3.1	72.8 \pm 1.0	50.8 \pm 4.1
Deep Sets w/ VarPool	60.0 \pm 3.8	73.8 \pm 0.9	56.1 \pm 3.0
Attn MeanPool	59.2 \pm 3.7	73.0 \pm 1.2	52.0 \pm 2.3
Attn MeanPool w/ VarPool	60.4 \pm 3.9	73.6 \pm 1.0	56.3 \pm 2.3
DeepGraphConv	57.9 \pm 4.2	70.7 \pm 2.3	51.4 \pm 3.0
DeepGraphConv w/ VarPool	58.0 \pm 5.2	70.9 \pm 2.3	51.6 \pm 3.2
	BLCA	UCEC	Overall
Deep Sets	56.6 \pm 5.3	51.3 \pm 4.3	58.2
Deep Sets w/ VarPool	57.5 \pm 5.1	54.1 \pm 3.0	60.3
Attn MeanPool	57.2 \pm 5.3	50.7 \pm 3.9	58.4
Attn MeanPool w/ VarPool	57.8 \pm 4.6	52.5 \pm 3.7	60.1
DeepGraphConv	52.1 \pm 7.7	54.2 \pm 2.1	57.3
DeepGraphConv w/ VarPool	53.1 \pm 7.6	55.0 \pm 2.0	57.7

This might lead to the development of multiple subclones of tumor cells that have different morphologies, as the effects of those mutations propagate from DNA to protein.

4 Interpretability and biological insights

This section presents two interpretability approaches to probe what biological signals the trained models learn. We focus on the Attention MeanPool and VarPool architectures, though similar approaches can be used for other architectures.

Interpretability via attention scores For each patient, we visualize the patches with the largest attention scores, i.e., the a in (1) and (3), as depicted in Figure 2. Note that this interpretability approach is not possible for the Deep Sets framework, since the attention weights are set to be uniform.

Interpretability via variance projection scores For variance pooling, we can examine signals captured by each variance pool projection. Each projection can be viewed as sorting the patches of a WSI, the biological signal of which we aim to uncover. We project the patches onto a given projection vector and visualize the patches along the spectrum. A similar interpretability approach was taken in Carmichael et al. [2021]. Following (3), for a projection vector v and j th instance, we define the *signed attention weighted squared residuals* (SAsqR) as

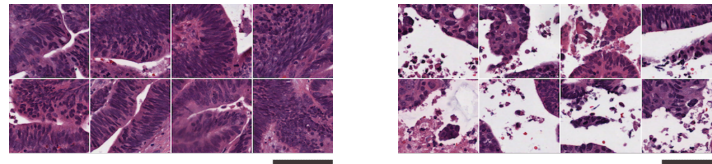
$$SAsqR_j = \text{sign}(r_j) a_j r_j^2, \text{ where } r_j := h_j^T v - \sum_{\ell=1}^n a_\ell h_\ell^T v.$$

These values can be used to sort the patches e.g. to identify the patches with the most extreme negative/positive SAsqR values.

4.1 Interpretability visualizations

We illustrate the two interpretability tools discussed in the previous section. Our analysis outputs a large number of images based on these tools. The figures below illustrate the trends that were reviewed by two pathologists.

Figure 2 compares the top attended patches for MeanPool and VarPool in one COADREAD patient. We observed that MeanPool attends to more compact, dense, and intact tumor with surrounding stroma, while VarPool attends to fragmented tumor, often with surrounding extracellular mucin and debris.

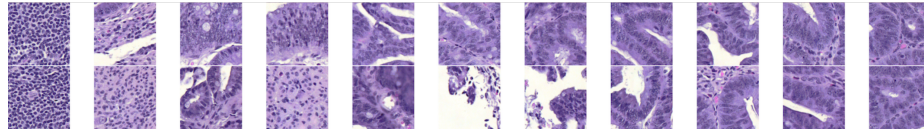


(a) Top MeanPool patches.

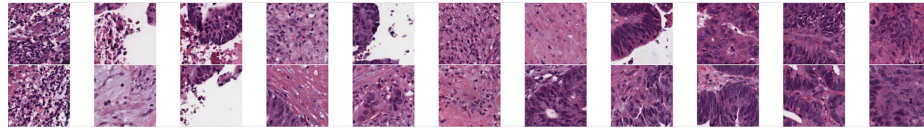
(b) Top VarPool patches.

Fig. 2: The highest attended patches for the attention MeanPool and VarPool for a single COADREAD patient. Here, MeanPool typically attends to solid tumor while VarPool attends to fragmented, more poorly-differentiated tumor. The scale bar represents $100 \mu m$.

Patient 1



Patient 2



low

SASqR

high

Fig. 3: Patches along one variance projection for two COADREAD patients. The patches are ordered from the most negative (left) SASqR scores to most positive (right). The leftmost patches contain dense inflammatory infiltrate comprised mostly of lymphocytes, while the rightmost patches show denser tumor regions.

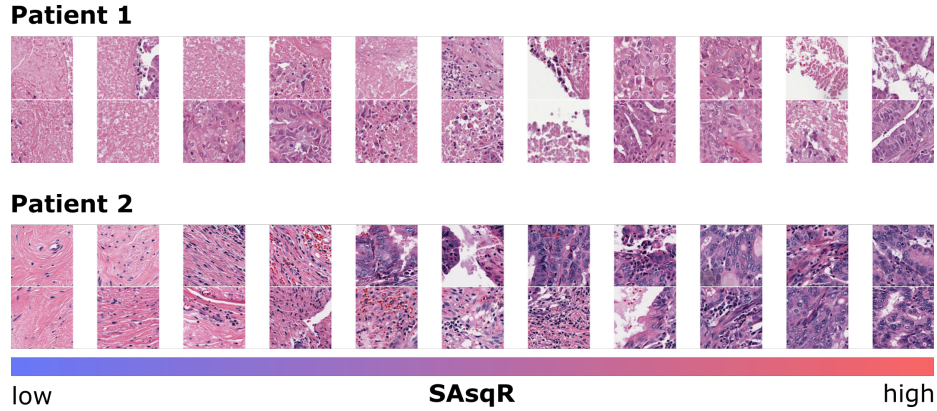


Fig. 4: Patches along one variance projection for two UCEC patients. This projection shows two patterns that are illustrated by these patients. For the first patient, the leftmost patches display necrosis and the right most patches display tumor. For the second patient, the leftmost patches display predominantly muscle and connective tissue and the right most patches display tumor.

Figure 3 shows patches along a single variance projection for two COAD-READ patients. Figure 4 is similar for UCEC. We have sorted the patches by their SAsqR values and shown several patches for 11 quantiles: 0, 10, ..., 100. We might expect the rightmost and leftmost patches to represent visual contrast. We observe dense tumor region on one end of the spectrum and other micro-environment features, such as lymphocytes, muscle, or necrosis on the other end.

5 Conclusion

We introduce a novel variance pooling module that can be incorporated into existing multiple instance learning (MIL) frameworks, to encode heterogeneity information through the second order statistics of low rank projections. We show that variance pooling can improve survival prediction across several cancer types. We also provide interpretability tools based on attention and projection scores to understand the heterogeneous biological signals captured by our framework. We hope this study will lead to further investigations of intratumoral heterogeneity – and other tumor microenvironment features – for computational pathology.

Acknowledgement

We thank Katherine Hoadley for helpful suggestions. This work was supported in part by internal funds from BWH Pathology, NIGMS R35GM138216 (F.M.), BWH President’s Fund, MGH Pathology, BWH Precision Medicine Program,

Google Cloud Research Grant, Nvidia GPU Grant Program and funding from the Fredrick National Lab. R.C. was additionally supported by the NSF graduate research fellowship. T.Y.C. was additionally funded by the NIH National Cancer Institute (NCI) Ruth L. Kirschstein National Service Award, T32CA251062. The content is solely the responsibility of the authors and does not reflect the official views of the NIH, NIGMS, NCI, or NSF.

Bibliography

- Noemi Andor, Trevor A Graham, Marnix Jansen, Li C Xia, C Athena Aktipis, Claudia Petritsch, Hanlee P Ji, and Carlo C Maley. Pan-cancer analysis of the extent and consequences of intratumor heterogeneity. *Nature medicine*, 22(1): 105–113, 2016.
- Gabriele Campanella, Matthew G Hanna, Luke Geneslaw, Allen Miralflor, Vitor Werneck Krauss Silva, Klaus J Busam, Edi Brogi, Victor E Reuter, David S Klimstra, and Thomas J Fuchs. Clinical-grade computational pathology using weakly supervised deep learning on whole slide images. *Nature Medicine*, 2019.
- Iain Carmichael, Benjamin C Calhoun, Katherine A Hoadley, Melissa A Troester, Joseph Geradts, Heather D Couture, Linnea Olsson, Charles M Perou, Marc Niethammer, Jan Hannig, et al. Joint and individual analysis of breast cancer histologic images and genomic covariates. *The Annals of Applied Statistics*, 15(4):1697–1722, 2021.
- Richard J Chen, Ming Y Lu, Muhammad Shaban, Chengkuan Chen, Tiffany Y Chen, Drew FK Williamson, and Faisal Mahmood. Whole slide images are 2d point clouds: Context-aware survival prediction using patch-based graph convolutional networks. In *MICCAI*, pages 339–349. Springer, 2021.
- Nicolas Coudray, Paolo Santiago Ocampo, Theodore Sakellaropoulos, Navneet Narula, Matija Snuderl, David Fenyö, Andre L Moreira, Narges Razavian, and Aristotelis Tsirigos. Classification and mutation prediction from non-small cell lung cancer histopathology images using deep learning. *Nature medicine*, 24(10):1559–1567, 2018.
- Pierre Courtiol, Charles Maussion, Matahi Moarii, Elodie Pronier, Samuel Pilcer, Meriem Sefta, Pierre Manceron, Sylvain Toldo, Mikhail Zaslavskiy, Nolwenn Le Stang, et al. Deep learning-based classification of mesothelioma improves prediction of patient outcome. *Nature medicine*, 25(10):1519–1525, 2019.
- Heather D Couture, Lindsay A Williams, Joseph Geradts, Sarah J Nyante, Ebonee N Butler, JS Marron, Charles M Perou, Melissa A Troester, and Marc Niethammer. Image analysis with deep learning to predict breast cancer grade, er status, histologic subtype, and intrinsic subtype. *NPJ breast cancer*, 4(1): 1–8, 2018.
- Kevin Faust, Adil Roohi, Alberto J Leon, Emeline Leroux, Anglin Dent, Andrew J Evans, Trevor J Pugh, Sangeetha N Kalimuthu, Ugljesa Djuric, and Phedias Diamandis. Unsupervised resolution of histomorphologic heterogeneity in renal cell carcinoma using a brain tumor-educated neural network. *JCO Clinical Cancer Informatics*, 4:811–821, 2020.
- Justin Guinney, Rodrigo Dienstmann, Xin Wang, Aurélien De Reynies, Andreas Schlicker, Charlotte Soneson, Laetitia Marisa, Paul Roepman, Gift Nyamundanda, Paolo Angelino, et al. The consensus molecular subtypes of colorectal cancer. *Nature medicine*, 21(11):1350–1356, 2015.

- Metin N Gurcan, Laura E Boucheron, Ali Can, Anant Madabhushi, Nasir M Rajpoot, and Bulent Yener. Histopathological image analysis: A review. *IEEE reviews in biomedical engineering*, 2:147–171, 2009.
- Maximilian Ilse, Jakub Tomczak, and Max Welling. Attention-based deep multiple instance learning. In *Proceedings of the 35th International Conference on Machine Learning*. PMLR, 2018.
- Douglas A Levine. Integrated genomic characterization of endometrial carcinoma. *Nature*, 497(7447):67–73, 2013.
- Jianfang Liu, Tara Lichtenberg, Katherine A Hoadley, Laila M Poisson, Alexander J Lazar, Andrew D Cherniack, Albert J Kovatich, Christopher C Benz, Douglas A Levine, Adrian V Lee, et al. An integrated tcga pan-cancer clinical data resource to drive high-quality survival outcome analytics. *Cell*, 173(2):400–416, 2018.
- Cheng Lu, David Romo-Bucheli, Xiangxue Wang, Andrew Janowczyk, Shridar Ganesan, Hannah Gilmore, David Rimm, and Anant Madabhushi. Nuclear shape and orientation features from h&e images predict survival in early-stage estrogen receptor-positive breast cancers. *Laboratory investigation*, 98(11):1438–1448, 2018.
- Ming Y Lu, Drew FK Williamson, Tiffany Y Chen, Richard J Chen, Matteo Barbieri, and Faisal Mahmood. Data-efficient and weakly supervised computational pathology on whole-slide images. *Nature biomedical engineering*, 5(6):555–570, 2021.
- Margaux Luck, Tristan Sylvain, Joseph Paul Cohen, Heloise Cardinal, Andrea Lodi, and Yoshua Bengio. Learning to rank for censored survival data. *arXiv preprint arXiv:1806.01984*, 2018.
- Andriy Marusyk, Michalina Janiszewska, and Kornelia Polyak. Intratumor heterogeneity: the rosetta stone of therapy resistance. *Cancer cell*, 37(4):471–484, 2020.
- Pooya Mobadersany, Safoora Yousefi, Mohamed Amgad, David A Gutman, Jill S Barnholtz-Sloan, José E Velázquez Vega, Daniel J Brat, and Lee AD Cooper. Predicting cancer outcomes from histology and genomics using convolutional networks. *Proceedings of the National Academy of Sciences*, 115(13):E2970–E2979, 2018.
- Franck Raynaud, Marco Mina, Daniele Tavernari, and Giovanni Ciriello. Pan-cancer inference of intra-tumor heterogeneity reveals associations with different forms of genomic instability. *PLoS genetics*, 14(9):e1007669, 2018.
- Yoni Schirris, Efstratios Gavves, Iris Nederlof, Hugo Mark Horlings, and Jonas Teuwen. Deepsmile: Contrastive self-supervised pre-training benefits msi and hrd classification directly from h&e whole-slide images in colorectal and breast cancer. *Medical Image Analysis*, 79:102464, 2022.
- Harald Steck, Balaji Krishnapuram, Cary Dehing-Oberije, Philippe Lambin, and Vikas C Raykar. On ranking in survival analysis: Bounds on the concordance index. *Advances in neural information processing systems*, 20, 2007.
- Ellery Wulczyn, David F Steiner, Melissa Moran, Markus Plass, Robert Reihs, Fraser Tan, Isabelle Flament-Auvigne, Trissia Brown, Peter Regitnig, Po-

- Hsuan Cameron Chen, et al. Interpretable survival prediction for colorectal cancer using deep learning. *NPJ digital medicine*, 4(1):1–13, 2021.
- Shekoufeh Gorgi Zadeh and Matthias Schmid. Bias in cross-entropy-based training of deep survival networks. *IEEE Transactions on Pattern Analysis and Machine Intelligence*, 43(9):3126–3137, 2020.
- Manzil Zaheer, Satwik Kottur, Siamak Ravanbakhsh, Barnabas Poczos, Russ R Salakhutdinov, and Alexander J Smola. Deep sets. In *Advances in Neural Information Processing Systems*, volume 30. Curran Associates, Inc., 2017.
- Yu Zhao, Fan Yang, Yuqi Fang, Hailing Liu, Niyun Zhou, Jun Zhang, Jiarui Sun, Sen Yang, Bjoern Menze, Xinjuan Fan, et al. Predicting lymph node metastasis using histopathological images based on multiple instance learning with deep graph convolution. In *Proceedings of the IEEE/CVF Conference on Computer Vision and Pattern Recognition*, pages 4837–4846, 2020.
- Xinliang Zhu, Jiawen Yao, Feiyun Zhu, and Junzhou Huang. Wsisa: Making survival prediction from whole slide histopathological images. In *Proceedings of the IEEE Conference on Computer Vision and Pattern Recognition*, pages 7234–7242, 2017.

Appendix

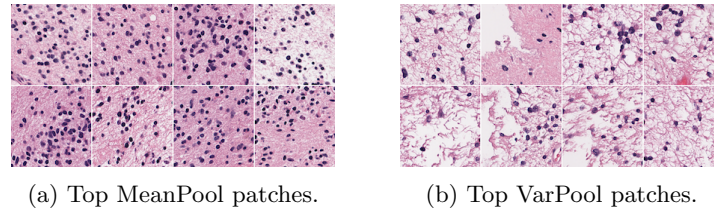


Fig. 5: The highest attended patches for the attention MeanPool and VarPool for a single GBMLGG patient. MeanPool attends to patches with high tumor cellularity, while VarPool attends to patches with lower cellularity.

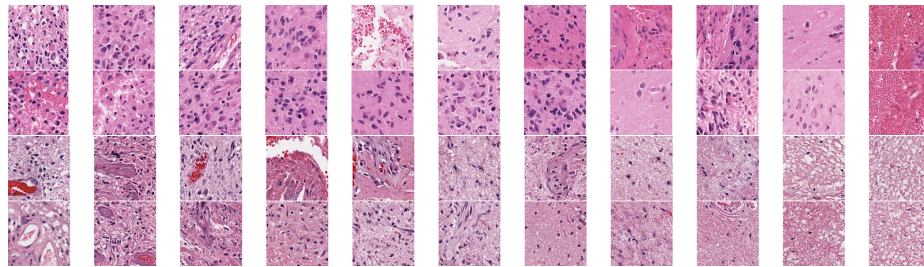


Fig. 6: Patches along one variance projection for two GBMLGG patients. As in the main body, the patches are ordered from the most negative (left) SASqR scores to most positive (right). The top patient is the patient predicted to have a high risk score, while the bottom patient is predicted to have a low risk score. This projection sorts the patches from lower cellularity (right) to higher cellularity (left) – recall we focus on the right/left extremes.

Table 2: Loss function ablation study. Test set c-Index performance (mean \pm std) on the 100 point scale for **cox loss**, where the training details were the same as the rank loss experiment. This shows that the variance pooling mechanism is loss-agnostic, equally showing improvement for both rank and cox loss.

Frameworks	BRCA	GBMLGG	COADREAD
Deep Sets	60.34 \pm 4.45	72.76 \pm 1.13	54.01 \pm 2.6
Deep Sets w/ VarPool	60.96 \pm 5.41	73.88 \pm 1.26	57.95 \pm 3.01
Attn MeanPool	59.89 \pm 4.51	73.25 \pm 1.16	54.71 \pm 2.55
Attn MeanPool w/ VarPool	61.1 \pm 4.48	73.21 \pm 1.18	58.49 \pm 3.12
DeepGraphConv	57.62 \pm 4.95	71.26 \pm 2.3	56.03 \pm 2.59
DeepGraphConv w/ VarPool	59.78 \pm 5.2	71.15 \pm 2.34	56.23 \pm 3.3
	BLCA	UCEC	Overall
Deep Sets	56.82 \pm 4.31	52.05 \pm 4.35	59.20
Deep Sets w/ VarPool	57.59 \pm 3.84	55.14 \pm 3.43	61.10
Attn MeanPool	56.95 \pm 4.26	51.16 \pm 2.85	59.19
Attn MeanPool w/ VarPool	57.47 \pm 3.43	53.53 \pm 3.49	60.76
DeepGraphConv	52.35 \pm 7.1	51.15 \pm 1.89	57.68
DeepGraphConv w/ VarPool	52.52 \pm 5.96	53.2 \pm 2.33	58.58

Table 3: The summary statistics for number of instances per WSI slide in the TCGA dataset. For training, we restricted the number of instances per slide to the 75% quantile for each cancer type. To fit a batch in one tensor, zero-padding and manually zeroing the attention was required for slides with fewer instances. For slides with more instances, we performed random subsampling. These measures were necessary to perform training with minibatches of slides (instead of batch size of 1 slide, as typically done in the literature).

	BRCA	GBMLGG	COADREAD	BLCA	UCEC
mean	10,826.28	7,448.28	8,575.54	16,599.11	16,003.92
median	10,388	4,661	5,535	16,742	16,856
75% quantile	14,871	11,803	14,076	20,766	21,624
min	260	23	174	491	458
max	67,268	36,996	36,495	39,793	45,482
std	6,999.84	6,847.36	6,799.17	7,118.88	8,219.33